J. Fluid Mech. (2025), *vol.* 1020, A14, doi:10.1017/jfm.2025.10640

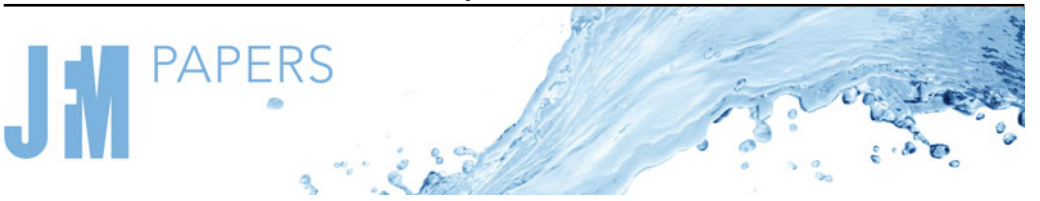

The non-dimensional parameters influencing tip leakage noise

Ivan Saraceno[1], **Paruchuri Chaitanya**[1] **and Bharathram Ganapathisubramani**[2]

[1]Institute of Sound and Vibration Research, University of Southampton, Southampton, UK

[2]Department of Aeronautics & Astronautics, University of Southampton, Southampton, UK

Corresponding authors: Ivan Saraceno, i.saraceno@soton.ac.uk; Paruchuri Chaitanya, C.C.Paruchuri@soton.ac.uk

(Received 24 March 2025; revised 9 July 2025; accepted 25 August 2025)

Tip leakage noise is one of the least understood noise sources in turbomachinery, arising from the interactions between the tip leakage flow, blade tips and casing boundary layer. This study employs experimental and parametric investigations to systematically identify three key non-dimensional parameters that govern tip leakage noise: the angle of attack α, the ratio between the maximum aerofoil thickness and gap size τ_{max}/e and between the gap size and boundary-layer thickness e/δ. These parameters regulate two fluid-dynamic instabilities, vortex shedding and shear-layer roll-up, responsible for the two tip leakage noise sources. Specifically, the first noise source arises when $\tau_{max}/e < 4$ and with the tip vortex positioned away from the aerofoil surface for $\alpha \geqslant 10°$. The second noise source occurs whenever the tip flow separates at the pressure side edge, with its strength proportional to the lift coefficient, depending on α, and diminishing as e/δ decreases and τ_{max}/e increases. Additionally, a relationship between the first noise source and drag losses is established, demonstrating that these losses are governed by α and τ_{max}/e.

Key words: aeroacoustics, shear layers, vortex shedding

1. Introduction

This study identifies the key parameters influencing tip leakage noise, which originates in the small gap between a ducted fan rotor and its surrounding casing. This region is also a source of two other broadband noise mechanisms: fan–boundary layer interaction noise and trailing-edge noise (Ganz *et al.* 1998). However, the distinction between these noise sources in a representative fan rig has been a persistent challenge. Grilliat *et al.* (2007) developed an experimental set-up with a single stationary aerofoil positioned in the core

of a wind tunnel jet to focus specifically on the tip leakage noise. According to Jacob *et al.* (2010), the physical mechanisms responsible for the tip noise in this set-up are similar to those observed in real fans.

Tip leakage noise arises from interactions between the tip leakage flow, which develops within the gap due to the pressure difference between an aerofoil's pressure and suction sides, the blade tip and the casing wall boundary layer. The tip leakage flow also interacts with the incoming flow, forming a vortex structure known as a tip leakage vortex (TLV). Two distinct tip leakage noise sources were identified, both linked to flow separation at the pressure side tip (Camussi *et al.* 2010; Jacob *et al.* 2010). According to Liu *et al.* (2024), this separation excited an unsteadiness that is sustained by its interaction with the incoming flow, propagating into the TLV core.

1.1. *Authors' prior works on tip leakage noise mechanisms*

Saraceno *et al.* (2024*b*) experimentally identified the fluid-dynamic instabilities responsible for two dipole-type tip noise sources, vortex shedding and shear-layer roll-up, using a set-up similar to that of Grilliat *et al.* (2007), the details of which are presented in § 2. Both instabilities were linked to the behaviour of the tip flow after its separation at the pressure side edge. Vortex shedding occurs when the tip flow does not reattach to the aerofoil, and within the non-dimensional frequency range $St_c = fc/U_0 = 2{-}5.5$. In contrast, shear-layer roll-up develops regardless of whether the tip flow reattaches or remains separated, within $St_c = 5.5{-}13$. Here, f is the frequency, c is the chord length and U_0 is the inflow velocity. The frequency content of the first noise source was found to vary with the chordwise position of the extended separated flow, which shifts based on the angle of attack and gap size. In contrast, the second noise source produces multiple spectral peaks that remain repeatable across different configurations. Similar trends in flow behaviour and acoustic signatures were observed across a range of inflow velocities, from 20 to 70 m s^{-1}, indicating that flow instabilities remain unchanged within the corresponding limited range of Reynolds number, $Re_c = U_0 c/\nu$ with ν the kinematic viscosity. Moreover, the occurrence of the same noise sources at consistent Strouhal numbers confirmed that the tip leakage noise is a Strouhal-dependent phenomenon.

These two fluid-dynamic instabilities were further investigated in Saraceno *et al.* (2024*a*), where large-eddy simulations were employed to analyse the two aerofoil cross-sections exhibiting different tip flow behaviours: from reattachment to extended separated flow. The numerical results not only confirmed the presence of these instabilities but also provided a definite overview of the tip leakage flow. Representative visualisations of these instabilities are shown in figures 1(*a*) and 1(*b*), based on experimental and numerical data, respectively. Specifically, figure 1(*a*) shows a large-scale coherence pattern starting downstream of the midchord, obtained by correlating the velocity fluctuations, measured using particle image velocimetry within the gap, with the far-field pressure signals, which have been band-pass-filtered within the range $St_c = 2{-}5.5$, corresponding to the frequency range of the first tip noise source. This pattern, captured by the first two proper orthogonal decomposition modes, was associated with the vortex-shedding mechanism. Figure 1(*b*) displays a pattern of smaller-scale structures that grow in size from the pressure to the suction side of the aerofoil, indicative of the shear-layer roll-up. This figure was obtained by applying spectral proper orthogonal decomposition on the midchord cross-section and at the non-dimensional frequency $St_c = 10$, which falls within the range of the second noise source, 5.5−13. The current study builds upon our previous works by systematically investigating the key non-dimensional parameters governing tip leakage flow and, consequently, the associated noise sources.

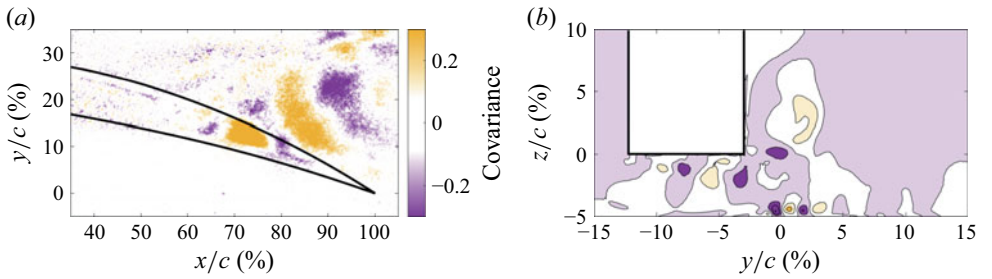

Figure 1. (*a*) Covariance plot obtained by relating the velocity fluctuation, measured using particle image velocimetry within the gap, with the far-field pressure signals filtered in the non-dimensional frequency range of the first noise source, $St_c = 2{-}5.5$. (*b*) Leading spectral proper orthogonal decomposition mode of the midchord section for the non-dimensional frequency $St_c = 10$, within the range of the second noise source, $St_c = 5.5{-}13$.

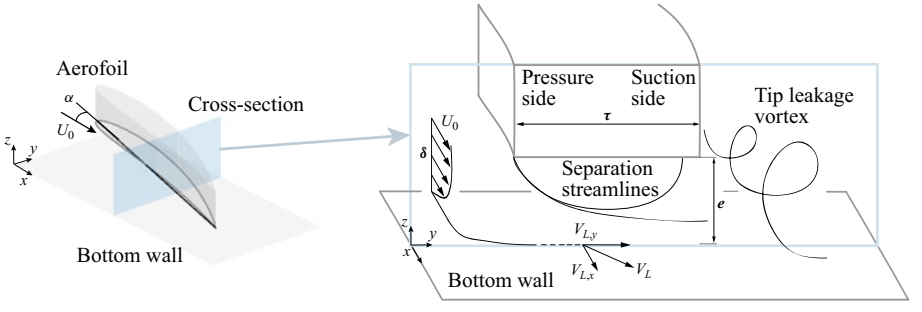

Figure 2. Schematic representation of the parameters influencing tip leakage flow. On the left, a global view of the test geometry, including coordinate axes, inflow direction U_0 and geometric angle of attack α. On the right, a zoomed-in sketch illustrating a generalised local cross-section of the aerofoil, highlighting key parameters: aerofoil thickness τ, gap size e, incoming boundary-layer thickness δ and the TLV forming on the suction side. The tip flow velocity close to the bottom wall is denoted with V_L.

1.2. *Key parameters influencing tip leakage flow*

The behaviour of the tip leakage flow plays a crucial role in the generation of associated tip noise sources. While past studies have identified certain dependencies of the tip leakage flow, the exact nature of their influence has remained largely unexplored. This work systematically investigates these dependencies and their interactions to establish their role in tip leakage noise generation. Figure 2 illustrates a global schematic of the test geometry, along with a zoomed-in view of a representative cross-section that highlights the parameters suggested to influence the tip leakage flow. The flow behaviour can vary depending on whether the section is characterised by a certain thickness-to-gap ratio τ/e, and the section's position relative to the TLV, which is influenced by the angle of attack α and the gap size e. The tip flow can also be influenced by whether the aerofoil tip is immersed in the casing boundary layer of thickness δ.

These geometric parameters can be defined *a priori*, unlike the characteristic length scales associated with the fluid instabilities responsible for the two noise sources (Saraceno *et al.* 2024*b*): the extension of the separated flow v in the spanwise direction, linked to the vortex shedding and associated with the non-dimensional frequency $St_v = fv/U_0 = 0.07$, and the shear-layer thickness b, associated with the roll-up and $St_b = fb/U_{SL} = 0.2$ with $U_{SL} \approx 0.5U_0$. However, the results reported in this paper show that the geometric

parameters affect the tip leakage flow and noise, thus offering a physically grounded yet practical framework to generalise the tip flow behaviour and associated noise mechanisms.

Storer & Cumpsty (1991) observed that the tip leakage flow does not reattach at the aerofoil downstream of the position of the minimum pressure measured on the endwall. This behaviour was suggested to be related to the ratio between the blade thickness τ and tip gap size e, which was at most 2.5, a value significantly lower than 7 measured by Moore & Tilton (1988), where the tip flow was observed to reattach to the aerofoil at the location downstream of the minimum pressure on the suction side. Graham (1986) measured the velocity profiles at a location close to the aerofoil suction side for three gap sizes, ranging from $\tau/e = 2.5$ to 5.2. The flow did not reattach in the configuration with the largest gap size, whereas a fully developed profile was observed for the smallest-gap-size case. The thickness-to-gap ratio was measured perpendicular to the chamberline, as Rains (1954) noted that the pressure gradient across the aerofoil is significantly larger than that along the chord, causing the tip flow to enter the clearance in a direction normal to the camber line. Denton (1993) suggested $\tau/e = 4$ as a threshold based on these past studies, indicating that for $\tau/e > 4$, typical in turbines, the tip flow generally reattaches before leaving the gap, whereas in compressors, where this ratio is often lower, reattachment is unlikely. Dambach & Hodson (2001) found even higher ratio, between 5 and 6, for a rotating blade. However, these studies (Graham 1986; Storer & Cumpsty 1991; Dambach & Hodson 2001) were carried out using a single aerofoil while varying only the gap size. One of the key contributions of this study is demonstrating the significance of the thickness-to-gap ratio by varying both aerofoil thickness and gap size, and quantifying its impact on the tip leakage flow and associated noise.

Storer & Cumpsty (1991) also observed that upstream of the position of minimum pressure measured on the wall, which corresponds with the trajectory of the TLV, the nature of the tip flow differed, with the flow reattaching to the aerofoil. Specifically, Intaratep (2006) found that the minimum pressure measured along the aerofoil suction side coincides with the position where the vortex begins to separate from the aerofoil surface. As the tip gap increases, the vortex moves further downstream, similar to when decreasing the angle of attack, as noted by Kang & Hirsch (1994). Saraceno *et al.* (2024*b*) suggested an interaction between the moving away of the vortex from the aerofoil surface and the onset of extended separated flow, as indicated by a shift in the pressure peak in the pressure distribution C_p that corresponds to a relocation of the extended separated region. However, due to the lack of TLV measurements, this interaction could not be confirmed in that study, but it is demonstrated as a novel finding in the current work.

Regarding the casing boundary layer, Zhang *et al.* (2022) observed that its interaction with the tip flow resulted in weakened pressure fluctuations near the onset of the TLV. To investigate this interaction, the aerofoil tip was immersed within the boundary layer, resulting in a ratio of gap to boundary-layer thickness $e/\delta < 1$. This differs from past investigations (Moore & Tilton 1988; Storer & Cumpsty 1991), where the gap size was larger than the boundary layer. According to Jacob *et al.* (2016*a*), a thinner boundary layer reduces the interaction noise between the upstream turbulence and the aerofoil leading edge, which might be responsible for a large part of the background noise masking the tip leakage noise in their pressure measurements.

The presence of the extended separated flow has been extensively studied due to its role in efficiency losses. Indeed, Bindon (1989) first identified that most losses occur when the separated bubble, localised near the pressure side edge, exits the gap. The concept of drag as a measure of lost performance has been applied to turbomachinery flows from external aerodynamics, as discussed by Denton (1993), who reviewed the loss mechanisms in turbomachines, defining 'loss' as any flow features that reduce their efficiency. Focusing

on tip leakage losses, lift losses always occur at the blade tip, due to both the reduction in blade length and the decrease in blade loading towards the tip. The analysis of the aerodynamic forces acting on the aerofoil has allowed the identification of a link between the first noise source and drag losses, never identified before.

1.3. *Contributions of the current study*

Our past investigations identified two tip leakage noise sources for a single stationary aerofoil, specifically attributed to fluid-dynamic instabilities developing within the tip gap: vortex shedding and shear-layer roll-up. These instabilities were connected to the behaviour of the tip flow after it separates at the pressure side tip. If the flow does not reattach to the aerofoil, both instabilities occur; if reattachment occurs, only roll-up is observed.

In this work, a systematic parametric study was carried out, analysing a wide range of configurations combining six distinct aerofoils, various gap sizes, seven angles of attack for each configuration and two boundary-layer thicknesses. This extensive analysis led to the identification of three key non-dimensional parameters influencing tip leakage flow and associated noise sources: angle of attack α, maximum thickness-to-gap ratio τ_{max}/e and ratio of gap to boundary-layer thickness e/δ. These parameters govern the pressure fluctuations $\overline{p'^2}$ associated with the tip leakage noise sources according to the following relationship:

$$\overline{p'^2} \propto f(\alpha, \tau_{max}/e, e/\delta). \tag{1.1}$$

The influence of the Reynolds number Re_c was found to be negligible within the range of tested inflow velocity, corresponding to $2.8 \times 10^5 < Re_c < 9.8 \times 10^5$, also suggesting tip leakage noise is a Strouhal-dependent phenomenon, as shown in Saraceno *et al.* (2024*b*).

The first noise source develops when $\tau_{max}/e < 4$ and with the TLV away from the aerofoil surface for $\alpha \geqslant 10°$. The location of the vortex detachment from the aerofoil surface can be identified by the minimum pressure peak in the pressure distribution C_p along the aerofoil suction side tip. The magnitude of this peak, directly linked to the noise source strength, depends on the three non-dimensional parameters. The second tip noise source occurs whenever the tip flow separates at the pressure side. Its strength is mainly proportional to the lift coefficient C_l, depending on α, and it decreases as e/δ decreases and τ_{max}/e increases. Furthermore, a relationship between the first noise source and drag losses is suggested, with these losses being a function of the angle of attack and thickness-to-gap ratio.

This paper is structured as follows. In § 3, the influence of the angle of attack on the tip noise sources is investigated for configurations with the same aerofoil and boundary-layer thickness (NACA 5510 and $\delta = 5$ mm). These initial findings are then generalised by considering different aerofoils, emphasising the impact of the thickness-to-gap ratio in § 4, which also includes an analysis of the aerodynamic forces acting on the entire aerofoil. The influence of boundary-layer thickness is discussed through these sections and is completed by examining another boundary-layer thickness in § 5.

2. Experimental set-up and flow characterisation

2.1. *Set-up*

Flow, pressure and force measurements were carried out to assess the influence of three non-dimensional parameters controlling the tip leakage flow and associated noise sources: the geometric angle of attack α, the ratio of the maximum aerofoil thickness to gap

	$\tau_m/e=1$	$\tau_m/e=2$	$\tau_m/e=3$	$\tau_m/e=4$	$\tau_m/e=5$	$\tau_m/e=6$
5505	$e=10$	$e=5$	$e=3.3$	$e=2.5$	$e=2$	$e=1.6$
5507	$e=14$	$e=7$	$e=4.6$	$e=3.5$	$e=2.8$	$e=2.3$
5510	$e=20$	$e=10$	$e=6.6$	$e=5$	$e=4$	$e=3.3$
5512	$e=24$	$e=12$	$e=8$	$e=6$	$e=4.8$	$e=4$
5515	$e=30$	$e=15$	$e=10$	$e=7.5$	$e=6$	$e=5$
5520		$e=20$	$e=13$	$e=10$	$e=8$	$e=6.6$

Table 1. List of all of the configurations analysed.

size τ_{max}/e and the ratio of gap size to boundary-layer thickness e/δ. To achieve this, configurations with aerofoils of different maximum thicknesses, gap sizes and angles of attack were analysed.

The set-up follows a similar design developed by Grilliat *et al.* (2007). It consists of an interchangeable aerofoil, with a chord length of $c = 200$ mm, positioned in the potential core of an open-jet wind tunnel between two Plexiglas plates, which are fixed at the top and the bottom of the nozzle exit. This set-up also allows for adjustments in the gap size e between the bottom wall and the aerofoil tip, as well as the geometric angle of attack α, defined as the angle between the aerofoil chord line and the inflow direction. The coordinate system used hereafter is based on the inflow direction: the x axis is aligned with it, pointing from the aerofoil leading edge to the trailing edge; the y axis is in the cross-stream direction, oriented from the pressure to the suction side; and the z axis is oriented upwards from the bottom wall. The inflow velocity U_0 was set to 40 m s^{-1}, yielding a chord-based Reynolds number of $Re_c = 5.6 \times 10^5$ and a Mach number of $M = 0.12$. This choice was supported by previous results showing similar flow behaviour across the range 20–70 m s^{-1}.

Table 1 lists all the configurations analysed, obtained by combining six different NACA 'XXXX' aerofoils with various gap sizes e (in mm) to achieve a specific thickness-to-gap ratio τ_{max}/e. The NACA four-digit series defines the aerofoil profile as follows: the first digit represents the maximum camber as a percentage of the chord, the second digit indicates the position of maximum camber in tenths of the chord and the last two digits specify the maximum thickness of the aerofoil as a percentage of the chord (Anderson 2001). A wide range of geometric angles of attack, $\alpha = 5°$, 7°, 10°, 12°, 15°, 17°, 20°, was considered. Analysing the effect of the boundary layer has been challenging due to the limitations of the current set-up. However, to address this, a duct of 2 m in length was added between the nozzle and the aerofoil, which increased the thickness of the turbulent boundary layer from 5 to approximately 20 mm, as shown in figure 3. This dimension was measured using a hot-wire at the location of the aerofoil leading edge, which had been removed.

The experiments were conducted at the Institute of Sound and Vibration Research's open-jet wind tunnel facility within an anechoic chamber measuring 8 m × 8 m × 8 m. The chamber's walls are acoustically treated with glass wool wedges, whose cut-off frequency is about 80 Hz. The nozzle has dimensions of 150 mm × 450 mm and a contraction ratio of 25 : 1. To ensure that the acoustic signature of the tip leakage noise can be clearly captured, the background noise remains at least 10 dB below the aerofoil self-noise, preventing contamination from facility noise, and the free-stream turbulence intensity is kept below 0.4 % in the potential core to minimise aerofoil–turbulence interaction noise. Further details of the facility are provided by Chong, Joseph & Davies (2009).

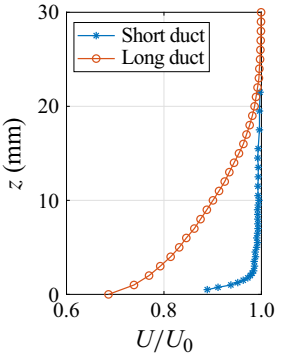

Figure 3. Streamwise velocity profile measured at the leading edge of the aerofoil for $U_0 = 40\ \mathrm{m\,s^{-1}}$.

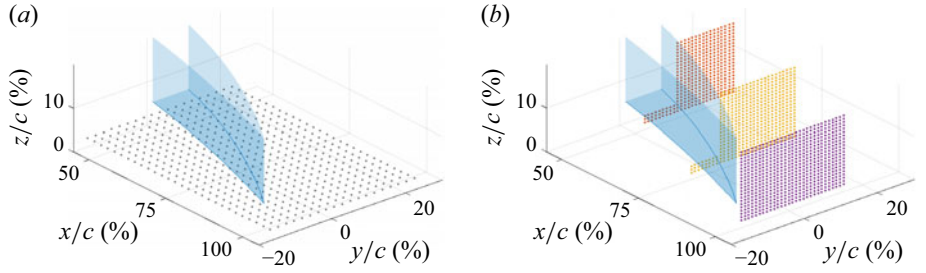

Figure 4. Schematic representations of the regions assessed using the hot-wire: (*a*) within the gap and (*b*) in the suction-side region.

2.2. *Type of measurements*

2.2.1. *Velocity*

Flow measurements were conducted to characterise the tip leakage flow within the gap and the TLV developing in the suction-side region of the aerofoil. The velocity field was assessed in a midgap plane and at different chordwise sections in the suction side using the hot-wire anemometry technique, as shown in figures 4(*a*) and 4(*b*). In both cases, the single-wire probe was oriented parallel to the x axis to measure the resultant velocity in the $x-z$ plane, i.e. $\sqrt{u^2 + w^2}$. Hot-wire anemometry has known limitations in regions of separated flow. We specifically targeted the low-velocity region within the gap, which we previously found to be associated with vortex-shedding instability responsible for the first tip noise source (Saraceno *et al.* 2024*b*). In the suction-side region, the measurements aimed to localise the TLV trajectory, as Jacob *et al.* (2016*b*) observed maximum axial velocities in the vortex core, further supporting the usefulness of the chosen probe orientation.

A single hot-wire probe (Dantec type 55P11) was operated using a standard constant-temperature anemometry system (AA Lab System) operated at an over-hear ratio of 1.5. It was calibrated in the free stream using a standard Pitot tube, with a fourth-order polynomial applied as a calibration function. The probe acquired data at each grid point for 10 s at a sampling frequency of 50 kHz, ensuring convergence of the mean statistics.

2.2.2. *Pressure*

Steady and unsteady pressure measurements were conducted in both near-field and far-field regions to evaluate the pressure distribution along the aerofoil and the far-field noise

spectra. The pressure distribution C_p over the aerofoil was evaluated by connecting surface pinholes to a pressure scanner with thin capillary tubes. These pressure taps are located at midspan and 1 mm above the aerofoil tip on both aerofoil sides, at 12 different locations along the chord. The formula used to evaluate C_p is as follows:

$$C_p(x) = \frac{p(x) - p_\infty}{0.5\rho_\infty U_0^2}, \tag{2.1}$$

where p_∞ is the pressure measured without flow, ρ_∞ is the density and U_0 is the inflow velocity. The lift coefficient C_l is obtained by numerically integrating the pressure distributions along the chord:

$$C_l = \int_0^c [C_{p_p}(x) - C_{p_s}(x)]\mathrm{d}(x), \tag{2.2}$$

where $C_{p_p}(x)$ and $C_{p_s}(x)$ represent the pressure distribution along the pressure and suction sides of the aerofoil, respectively.

Far-field noise measurements were performed using four half-inch condenser microphones (B&K type 4189) located at a radial distance of 1.5 m from the aerofoil midchord. Two microphones were placed on the suction side and two on the pressure side at polar angles of $\theta = \pm 90°$ and $\theta = \pm 40°$ relative to the inflow direction. However, only data from the pressure side microphone at $\theta = -90°$, where noise levels were highest, are reported. Far-field pressure signals were acquired for 10 s at a sampling frequency of 50 kHz. The noise spectra are calculated with Welch's method, using a window size of 1024 data points with no overlap. This corresponds to a frequency resolution of 48.83 Hz and a bandwidth–time product of 488.3, which is sufficient to ensure a 9 % uncertainty with a 95 % confidence level (Glegg & Devenport 2017).

2.2.3. *Aerodynamic forces*

A load cell was mounted to the aerofoil to measure the forces acting on it. Specifically, an F/T Sensor Mini40 is mounted between two steel brackets. Four adjustable bolts regulate the gap size and set the position of the upper bracket. The lower bracket is attached to the aerofoil but can move freely. This set-up ensures that the lower bracket transfers these forces to the load cell for measurement as the aerofoil moves under aerodynamic forces.

The forces of interest are lift L and drag D, which are non-dimensionalised as follows:

$$C_L = \frac{L}{0.5\rho_\infty U_0^2 S}, \tag{2.3}$$

$$C_D = \frac{D}{0.5\rho_\infty U_0^2 S}, \tag{2.4}$$

where S is the relevant surface area, calculated as the product of the aerofoil chord and the span length, which varies with the gap size. The load cell measures two forces: one perpendicular to the aerofoil chord and the other along it, F_1 and F_2, respectively. The lift and drag are then calculated from F_1 and F_2 as

$$L = F_1 \cos(\alpha_{eff}) - F_2 \sin(\alpha_{eff}), \tag{2.5}$$

$$D = F_1 \sin(\alpha_{eff}) + F_2 \cos(\alpha_{eff}), \tag{2.6}$$

where α_{eff} is the effective angle of attack of the aerofoil, which is lower than the geometric angle of attack α due to the wind tunnel deflection (Glegg & Devenport 2017). The jet can be deflected due to the presence of an aerofoil, leading to a reduction in the effective angle experienced by the aerofoil. This effective angle can be estimated by matching the

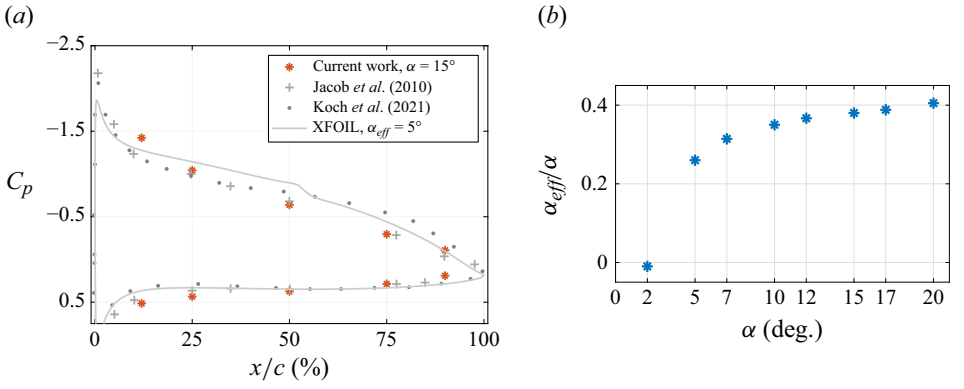

Figure 5. (*a*) Pressure distributions measured at midspan for $\alpha = 15°$ in the current work, compared with other results in the literature (Jacob *et al.* 2010; Koch, Sanjosé & Moreau 2021), and the numerical prediction from XFOIL for $\alpha_{eff} = 5°$. (*b*) Variation of the ratio α_{eff}/α with the geometric angle of attack α.

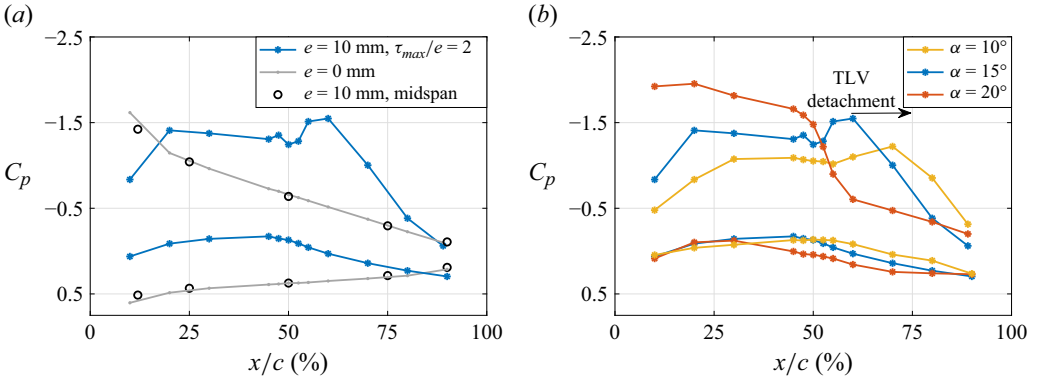

Figure 6. (*a*) Pressure distributions C_p along the aerofoil measured at the tip for two configurations with gap sizes $e = 0$ and 10 mm, and at midspan for $e = 10$ mm. The angle of attack is set to $\alpha = 15°$. (*b*) Pressure distribution C_p measured at the tip for three configurations with $\alpha = 10°$, 15° and 20°. The gap size is set to $e = 10$ mm, corresponding to $\tau_{max}/e = 2$.

experimental pressure distribution C_p, measured along the midspan where the tip flow effects are negligible (as shown in § 3), with the numerical predictions obtained using XFOIL (Drela 1989). Figure 5(*a*) compares the experimental C_p at $\alpha = 15°$ with the best matching numerical prediction obtained for $\alpha_{eff} = 5°$, along with additional measurements from the literature (Jacob *et al.* 2010; Koch *et al.* 2021). The ratio α_{eff}/α, shown in figure 5(*b*), exhibits a sharp increase between $\alpha = 2°$ and 5°, and then increases slightly for higher angles, assuming values of around 1/3.

3. Influence of the angle of attack α

3.1. *Tip leakage vortex detachment on tip-separated flow*

The pressure distributions C_p along the aerofoil measured close to the tip for two gap sizes $e = 0$ and 10 mm, and same angle of attack $\alpha = 15°$, are shown in figure 6(*a*), together with that evaluated at midspan for $e = 10$ mm. In the presence of the gap, the pressure distribution near the tip changes significantly compared with that at midspan, which corresponds to the loading at the tip without clearance in agreement with previous

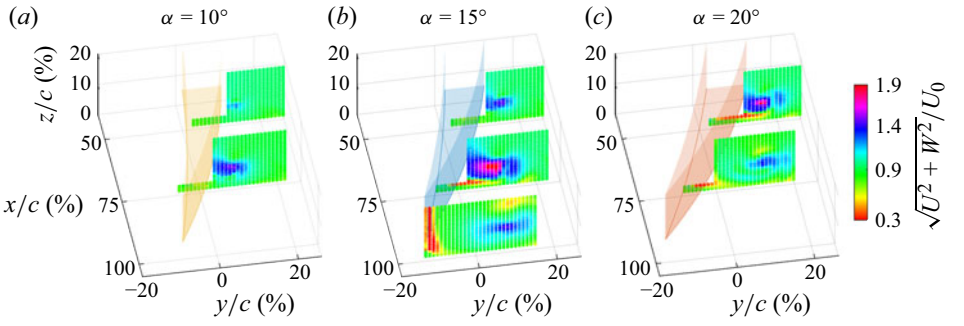

Figure 7. Mean velocity fields of the resultant velocity in the $x-z$ plane measured for three configurations with $\alpha = 10°$ (*a*), 15° (*b*) and 20° (*c*) in different chordwise sections: at midchord, at 75 % of the chord and at 2 mm downstream the trailing edge. The gap size is set to $e = 10$ mm, corresponding to $\tau_{max}/e = 2$.

studies (Jacob *et al.* 2010; Koch *et al.* 2021). This indicates that the gap mainly influences the pressure distribution near the tip edge. The loading on the pressure side tends to be lower in the presence of a gap, particularly upstream of the midchord. On the suction side, the pressure decreases downstream of the leading edge reaching a peak around the 60 % of the chord, followed by a subsequent drop. The magnitude of the peak and its location along the chord vary with changes in the angle of attack, as shown in figure 6(*b*). Specifically, when the angle of attach decreases from 20° to 10°, the magnitude of the peak on the suction side diminishes, and the drop shifts downstream, from midchord to 75 % of the chord.

Previous studies linked the loading on the aerofoil suction side to the TLV (Graham 1986; Kang & Hirsch 1993), which remains near the aerofoil surface. The pressure peak, followed by the drop, occurs when the vortex moves away from the surface (Intaratep 2006). According to figure 6(*b*), this vortex detachment shifts progressively upstream with the increase of the angle of attack. This behaviour is qualitatively shown in figure 7, which displays the resultant velocity contained in the $x-z$ plane measured by the hot-wire probe in different chordwise sections, precisely at $x/c = 50$ %, 75 % and at 2 mm downstream of the trailing edge, for the three configurations with $\alpha = 10°$, 15° and 20°. The resultant velocity reaches maximum values in the vortex core. The location of this maximum velocity indeed matches with the centre of the TLV identified by Jacob *et al.* (2016*a*) at the same chordwise section located downstream of the trailing edge, for the configuration with $\alpha = 15°$ shown in figure 7(*b*). For this configuration, the trajectory of the TLV can be qualitatively inferred from the three sections, showing that it is almost aligned with the inflow direction, consistent with other works (Jacob *et al.* 2016*b*; Koch *et al.* 2021). The vortex core remains close to the aerofoil suction side up to the midchord, and then it starts to move away, as expected from its pressure distribution ($\diamond$) in figure 6(*b*). For $\alpha = 10°$ in figure 7(*a*), the vortex core remains close to the aerofoil suction side up to 75 % of the chord, whereas for $\alpha = 20°$ in figure 7(*c*), the core begins to move away from the surface around the midchord. In summary, the relationship between the TLV and the pressure distributions on the aerofoil suction side is clear, with the location of vortex detachment shifting as the angle of attack changes. Furthermore, the vortex is located near the aerofoil tip, so it does not influence the pressure at the midspan. As a result, the pressure distribution at the midspan remains similar to that of the configuration without a gap, as seen in figure 6(*a*).

Hot-wire measurements were used to trace the vortex core in the suction-side area of the aerofoil and evaluate the flow within the gap. The tip flow exhibits low velocity values

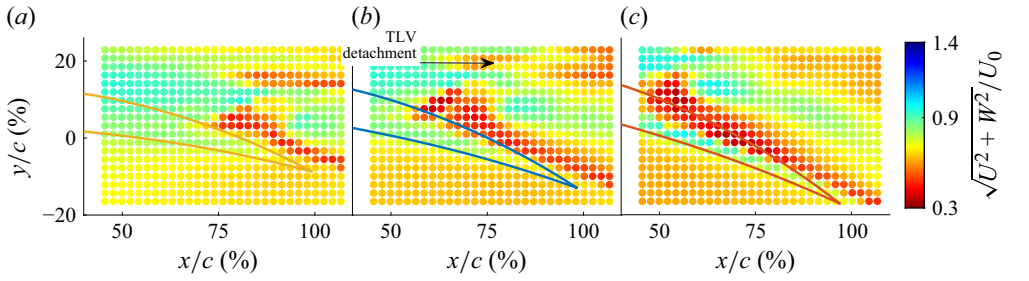

Figure 8. Mean velocity fields of the resultant velocity in the $x-z$ plane measured within the gap for three configurations with $\alpha = 10°$ (a), 15° (b) and 20° (c). The gap size is set to $e = 10$ mm, corresponding to $\tau_{max}/e = 2$. The colour map is chosen to maintain consistent colour representation of velocity values with figure 7.

at midchord for the configuration with $\alpha = 20°$ in figure 7(c), and at 75 % of the chord for $\alpha = 15°$ and 20°, in figures 7(b) and 7(c). Figure 8 displays this characteristic more clearly, showing the flow fields in the midgap plane for these three configurations with $\alpha = 10°$, 15° and 20°. The low-velocity regions, found for each case in figure 8, arise downstream of the pressure peaks identified in the pressure distributions in figure 6(b). The low-velocity region shifts upstream as the angle of attack increases, following the same shifting trend as the pressure peaks. Given the connection between the pressure peak and low-velocity region, as well as between the peak and vortex detachment, it can be suggested that the TLV plays a role in the development of the low-velocity region.

Saraceno *et al.* (2024*a*) used large-eddy simulations to investigate two chordwise sections of the configuration with $\alpha = 15°$, at midchord and at 75 % of the chord, of the configuration with $\alpha = 15°$. At midchord, the flow was found to separate at the tip but to reattach before leaving the gap. At 75 % of the chord, the tip flow remained separated until the exit of the gap and low axial velocity was measured. This low-velocity region corresponds to those observed in figures 7 and 8. Figure 7 also indicates that the extended separated flow occurs when the TLV is away from the aerofoil suction side. A similar trend was observed by Liu *et al.* (2024), who found an extended separation developed within the gap downstream of the TLV detachment from the aerofoil surface, while upstream, the flow remained steady and attached. This trend suggests that when the TLV is close to the aerofoil surface, its low pressure can influence the separated flow to reattach to the aerofoil tip. However, as the TLV moves away, this effect vanishes, and the tip flow stays separated until it exits the gap. Figure 8 also shows that the velocity values within the low-velocity region decrease as the angle of attack increases. This behaviour appears to be correlated with the intensity of the pressure peaks: as the pressure peak magnitude increases, the vortex is characterised by lower pressure, which may lead to a stronger separation upon its detachment.

Figure 9 shows the lift coefficient C_l as a function of the angle of attack α for different gap sizes e. The gap size has been non-dimensionalised using the maximum thickness of the 5510 aerofoil, i.e. $\tau_{max} = 20$ mm. The lift coefficient remains nearly constant as the gap size varies and for a fixed angle of attack. This is unexpected given that the pressure distributions with and without the gap differ significantly, as shown in figure 6(a). Based on this figure, it can be hypothesised that, to keep the lift coefficient constant, the loading on the pressure side is reduced in the presence of the gap to counterbalance the loading on the suction side caused by the TLV. However, the effect of the gap size on the lift coefficient becomes evident for large gaps ($\tau_{max}/e > 2$) and small angles of attack ($\alpha < 12°$), resulting in a significant reduction in lift.

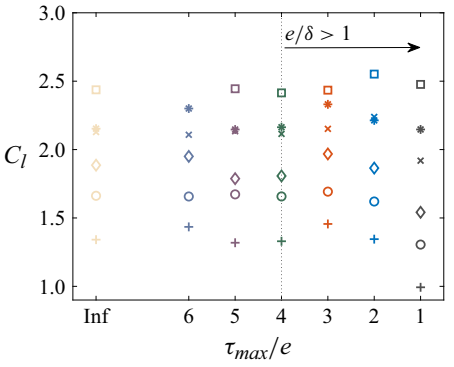

Figure 9. Lift coefficient C_l plotted against the non-dimensionalised gap size τ_{max}/e, obtained for different angles of attack. The markers refer to the angles of attack: plus, 5°; circle, 7°; diamond, 10°; cross, 12°; star, 15°; square, 17°.

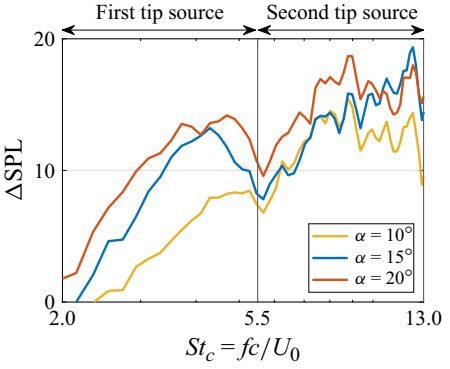

Figure 10. Tip leakage noise obtained by subtracting the sound pressure levels measured with and without the gap, for the three configurations with $\alpha = 10°$, 15° and 20° and gap size $e = 10$ mm, corresponding to $\tau_{max}/e = 2$.

3.2. *First tip noise source*

The focus on the low-velocity region is due to its association with a vortex-shedding-type phenomenon, which was identified as responsible for one of the tip leakage noise sources (Saraceno *et al.* 2024*a*,*b*). This noise source was linked to the spectral hump found in figure 10, within the non-dimensional frequency range $St_c = fc/U_0 = 2{-}5.5$. The curves plotted in this figure are obtained by subtracting the far-field spectra obtained with and without the gap to highlight the noise increase due to the tip leakage noise. This subtraction partially removes the contribution of other noise sources, such as background noise and leading- and trailing-edge noise, since these are expected to be similar with and without the gap. As the angle of attack decreases from 20° to 10°, the spectral hump narrows and its peak shifts towards higher frequencies. This behaviour was associated with the location where the low-velocity region starts to appear. As a result of the previous considerations, the first tip noise source depends on the TLV detachment location.

The peaks on the pressure distributions along the suction side have been linked to the flow separation: a higher peak indicates stronger separation, which may lead to more intense vortex-shedding phenomena responsible for the first tip noise source, explaining the louder spectral peak observed in figure 10 as the angle of attack increases.

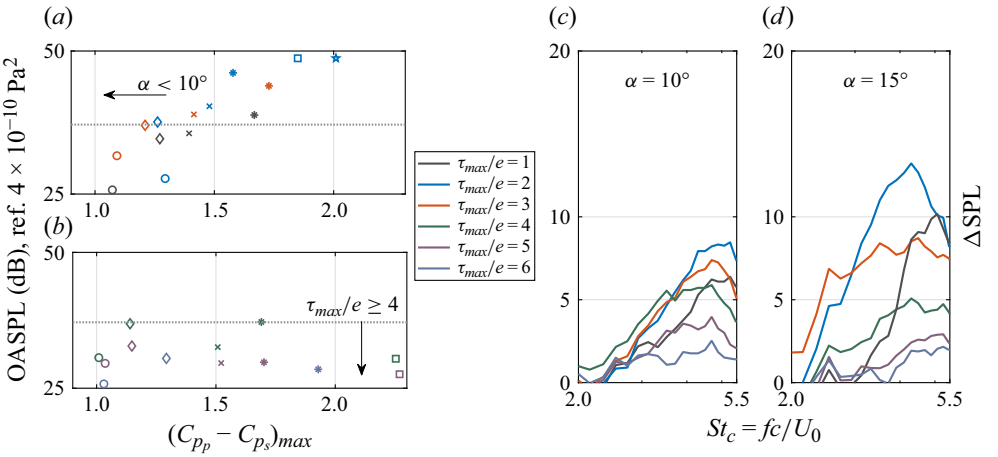

Figure 11. Overall sound pressure levels evaluated in the frequency range of the first tip noise source against the maximum difference between C_{p_p} and C_{p_s}, for different configurations characterised by $\tau_{max}/e = 1$, 2 and 3 (*a*), and $\tau_{max}/e = 4$, 5 and 6 (*b*). Tip leakage noise for different configurations with $\alpha = 10°$ (*c*) and 15° (*d*). The markers refer to the angles of attack: circle, 7°; diamond, 10°; cross, 12°; asterisk, 15°; square, 17°; star, 20°.

This relationship between pressure peak and noise strength is further shown in figure 11(*a*), where the spectral curves, integrated within the frequency range of the first noise source, are plotted as a function of the maximum pressure peak of the pressure distribution along the aerofoil suction side, C_{p_s}, on the abscissa. Specifically, the abscissa has been 'normalised' by considering the maximum difference between C_{p_p} and C_{p_s}, to account for the effect of the TLV on the pressure distribution of aerofoil pressure side C_{p_p}, as suggested previously. The blue data points in figure 11(*a*) correspond to the configurations with $e = 10$ mm, i.e. $\tau_{max}/e = 2$, for different angles of attack. The strength of the first noise source exhibits a sudden increase when passing from $\alpha = 7°$ to 10°, followed by a rise that reaches its maximum at $\alpha = 20°$. Beyond this point, stall occurs at $\alpha = 30°$, as reported by Saraceno *et al.* (2024*b*). The other cases shown in figure 11(*a*) with $\tau_{max}/e = 1$ and 3 display the same trend, albeit with lower maximum intensity. On the contrary, the points for the cases with $4 \leqslant \tau_{max}/e \leqslant 6$ mainly cluster below the dotted line in figure 11(*b*).

The clustering below the dotted line, along with the sudden drop in the noise strength at small angle of attack ($\alpha < 10°$), is associated with the absence of the first noise source. The dotted line is defined based on the observation that the case with $\tau_{max}/e = 4$ and $\alpha = 15°$ was found to exhibit neither the first noise source nor extended separated flow (Saraceno *et al.* 2024*b*). Figure 11(*d*) shows the tip leakage noise obtained for this case (–), along with those obtained for $1 \leqslant \tau_{max}/e \leqslant 6$. The spectral humps remain negligible, below 5 dB, for $\tau_{max}/e \geqslant 4$. Other data points are found along the dotted line for $\alpha = 10°$ in figures 11(*a*) and 11(*b*), and their tip noise spectra are shown in figure 11(*c*). The case with $\tau_{max}/e = 2$ (–) is characterised by a shallow spectral peak and low-velocity region, as seen in figure 8(*a*). This hump decreases as τ_{max}/e increases, approaching 5 dB for $\tau_{max}/e = 4$, and eventually becomes negligible, below 5 dB, for higher values. In summary, the first noise source does not develop for $\tau_{max}/e \geqslant 4$ and $\alpha < 10°$. The reason why the data for $\tau_{max}/e \geqslant 4$ collapse below the dotted line will be shown to be linked to the ratio between the aerofoil thickness and the gap size, despite these configurations having their tips immersed within the boundary layer. The absence of the first noise source for

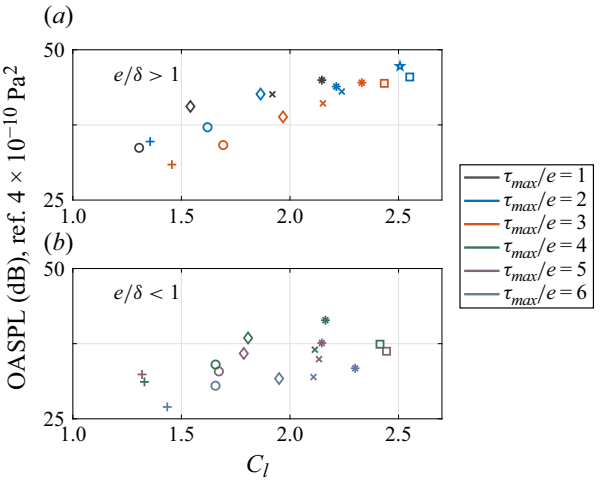

Figure 12. Overall sound pressure levels evaluated in the frequency range of the second noise source against the lift coefficient C_l measured at the tip for different configurations characterised by $\tau_{max}/e = 1$, 2 and 3 (*a*), and $\tau_{max}/e = 4$, 5 and 6 (*b*). The markers refer to the angles of attack: plus, 5°; circle, 7°; diamond, 10°; cross, 12°; asterisk, 15°; square, 17°; star, 20°.

$\alpha < 10°$ is attributed to the lack of extended separated flow, which may result from the vortex detachment occurring even further downstream of 75 % of the chord. Additionally, it should be considered that the tip flow changes as the angle of attack decreases, with a much weaker cross-stream flow forming even further downstream of 75 %, as observed by Jacob *et al.* (2010) for the configuration with $\alpha = 5°$ and $\tau_{max}/e = 2$.

3.3. *Second tip noise source*

The second tip noise source was associated with a shear-layer roll-up (Saraceno *et al.* 2024*a*,*b*), which develops within the gap due to the separation of the flow at the pressure side tip edge. Figure 10 identifies the noise increase due to this fluid-dynamic instability within $St_c = 5.5-13$. As the angle of attack increases, the levels rise reaching the greatest values for the configuration with $\alpha = 20°$. The integration of the curves in figure 10 over the corresponding frequency range of the second noise source results in the scatter plot of figures 12(*a*) and 12(*b*), where the abscissa represents lift coefficient C_l, obtained by integrating the pressure distributions along the chord. These figures have been enhanced with additional data points obtained by varying the angle of attack, between 5° and 20°, and gap size, in the range $1 \leqslant \tau_{max}/e \leqslant 6$. Specifically, the cases with $\tau_{max}/e \leqslant 3$, also characterised by the aerofoil tip outside the boundary layer $e/\delta > 1$, are shown in figure 12(*a*), while the others are presented in figure 12(*b*). Figure 12(*a*) shows a proportionality between the strength of the second tip noise source and the lift coefficient. In figure 12(*b*), for $e/\delta < 1$, the data appear slightly more dispersed but still show an increase of the noise source with the lift coefficient. A detailed analysis of these data, including the effects of the casing boundary layer, is conducted in the next sections.

The proportionality, shown in figure 12(*a*), between the overall loading acting on the aerofoil tip and the strength of the second tip noise source is not straightforward. This noise source was linked to the shear-layer roll-up, which develops from the separation of the flow entering the gap at the pressure side edge. The roll-up is due to the Kelvin–Helmholtz instability, which arises from a velocity difference across the interface of two parallel fluid streams (Kundu, Cohen & Dowling 2016). In the tip flow scenario, these streams are

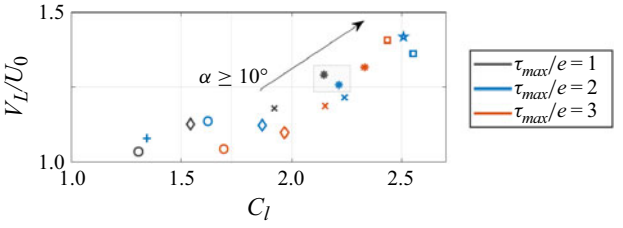

Figure 13. Tip flow velocity V_L plotted against the lift coefficient C_l, obtained for $\tau_{max}/e = 1,\ 2$ and 3. The markers refer to the angles of attack: plus, 5°; circle, 7°; diamond, 10°; cross, 12°; asterisk, 15°; square, 17°; star, 20°.

represented by the separated flow near the aerofoil tip and a high-speed jet flow close to the bottom wall, as depicted in the zoomed-in aerofoil cross-section in figure 2 and observed by Saraceno *et al.* (2024*b*) and Storer & Cumpsty (1991). Since the separated flow near the aerofoil has negligible velocity, the roll-up mechanism is primarily influenced by the flow velocity near the wall, V_L. A way to estimate of this velocity, normal to the chamber line, was provided by Rains (1954), using the following expression: $V_L/U_0 = \sqrt{C_{p_{p,m}} - C_{p_s}}$, where $C_{p_{p,m}}$ is the pressure coefficient measured at midspan on the aerofoil pressure side and C_{p_s} is that measured at the tip on the suction side. This formula was derived from the ideal model, proposed by Rains (1954), which applies the Bernoulli equation under the assumption of an ideal, unattached flow entering the gap normal to the chamber line. Consequently, as noted by Storer & Cumpsty (1991), this expression provides a good estimate of the flow velocity when applied to sections downstream of the minimum pressure on the suction side, where the flow tends to be unattached.

In this study, the flow velocity V_L is evaluated by considering the pressure coefficients measured at the location of the minimum pressure peak and at the aerofoil tip of both sides, using this formula $V_L/U_0 = \sqrt{C_{p_p} - C_{p_s}}$, where C_{p_p} is the pressure coefficient measured at the pressure side tip. The scatter plot of figure 13 displays V_L plotted against the lift coefficient C_l, obtained by varying the angle of attack for all the configurations with the aerofoil tip outside the boundary layer to satisfy the assumption of ideal flow, i.e. $e/\delta > 1$ corresponding to $1 \leqslant \tau_{max}/e \leqslant 3$. The data show a linear relationship between V_L and C_l, which is evident for $\alpha \geqslant 10°$, but not for lower angles of attack, $\alpha < 10°$. This discrepancy may be due to the method of evaluating V_L, which relies on pressure coefficients measured at the same chordwise location on both aerofoil sides, potentially causing inaccuracies in the velocity estimation at low angles of attack. At low angles of attack, the pressure tap locations almost align with the cross-stream direction, providing an estimate of the cross-stream flow, while the actual tip flow has both stream and cross-stream components, $V_{L,x}$ and $V_{L,y}$, as shown in figure 2. Additionally, at low angle of attack, the cross-stream flow is weaker, as observed by Jacob *et al.* (2010). As the angle of attack increases, the tip flow changes with a higher cross-stream component and the alignment of the pressure taps with the actual tip flow direction improves, leading to a more accurate estimation of V_L.

This section illustrates a linear relationship between the lift coefficient and the tip flow velocity, without claiming an exact value of V_L, due to the several assumptions inherent in the Rains model. This relationship helps to explain the connection between the lift coefficient and the strength of the second noise source observed in figure 12. As the lift coefficient increases, the greater pressure difference between the suction and pressure side results in a faster flow close to the bottom wall, enhancing the shear within the gap. This results in stronger shear-layer vortices, which in turn induce larger unsteady aerodynamic

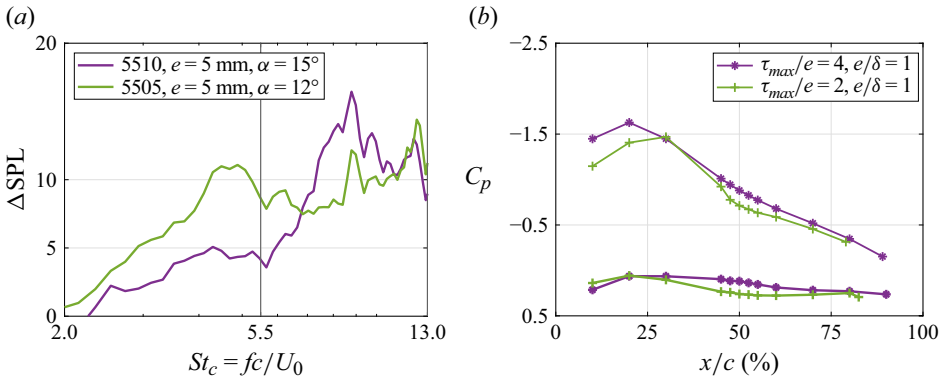

Figure 14. (*a*) Tip leakage noise and (*b*) pressure distributions C_p along the aerofoil measured at the tip for the two configurations with $\tau_{max}/e = 2$, 4 and angle of attack set to $\alpha = 12°$, 15°.

forces and, consequently, a more intense tip noise source. In § 4, a power relationship between lift coefficient and strength of the second noise source is presented.

4. Influence of the thickness-to-gap ratio τ/e

Denton (1993) suggested that the behaviour of the tip leakage flow is a function of the ratio between the local aerofoil thickness τ and gap size e. When $\tau/e > 4$, the tip flow typically reattaches before leaving the gap, while for lower values, the flow is unlikely to reattach to the blade. In the previous section, a 5510 NACA aerofoil with $\tau_{max} = 20$ mm localised at 30 % of the chord was considered. For the cases with non-dimensional gap sizes $\tau_{max}/e = 2$ shown in figure 7, this results in $\tau/e < 2$ along the entire chord, with the tip flow remaining separated unless the vortex is close to the aerofoil surface, which encourages the reattachment. This separation leads to the first tip noise source, which tends to disappear for non-dimensional gap sizes $\tau_{max}/e \geqslant 4$, as seen in figures 11(*a*) and 11(*b*). Given that the first tip noise source is intrinsically linked to the behaviour of the tip flow, this section investigates the influence of the thickness-to-gap ratio, by varying also the aerofoil thickness, on both first and second tip noise sources.

4.1. *First tip noise source*

Two different NACA aerofoils, 5505 and 5510 with $\tau_{max} = 10$ and 20 mm, at different angles of attack $\alpha = 12°$ and 15°, were analysed in detail. Both featured a gap size of $e = 5$ mm, corresponding to $e/\delta = 1$. Figure 14 displays the tip leakage noise and the pressure distribution C_p along the chord obtained for these two configurations with $\tau_{max}/e = 2$ and 4. Although the pressure distributions are nearly identical, only the configuration with $\tau_{max}/e = 2$ exhibits a distinct spectral hump in the frequency range of the first noise source, $St_c = 2{-}5.5$, with a peak of 11 dB. This noise source suggests the development of a low-velocity region, expected to form at the location where the vortex detaches. According to the pressure distributions in figure 14(*b*), the vortex detaches from the aerofoil surface around 25 % of the chord, corresponding to the location of the maximum aerofoil thickness. This detachment is confirmed in figure 15, which displays the resultant velocity in the $x{-}z$ plane measured at the midchord and 75 % of the chord. In both configurations, the trajectory of the vortex core, identified by maximum velocity values, is located further from the aerofoil surface in those sections downstream of 25 % of the chord. At 25 % of the chord, the difference between the two configurations is the

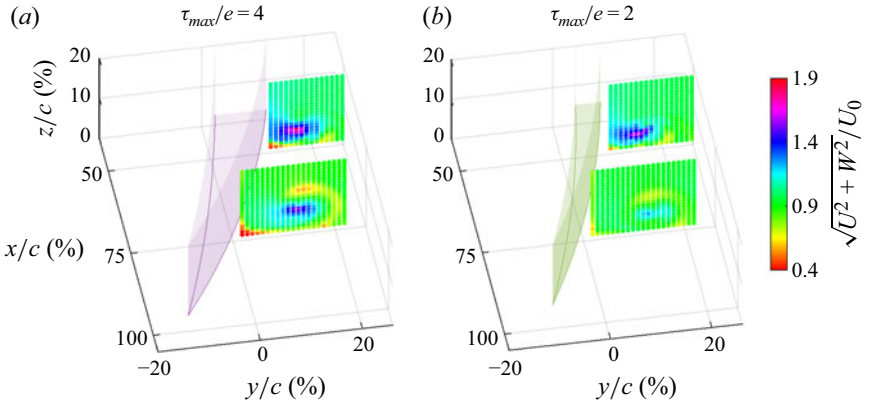

Figure 15. Mean velocity fields of the resultant velocity in the $x-z$ plane measured for two configurations with $\tau_{max}/e = 4$, $\alpha = 15°$ (*a*) and $\tau_{max}/e = 2$, $\alpha = 12°$ (*b*) in different chordwise sections, midchord and 75 % of the chord. Different aerofoils characterise these configurations, NACA 5510 and 5505.

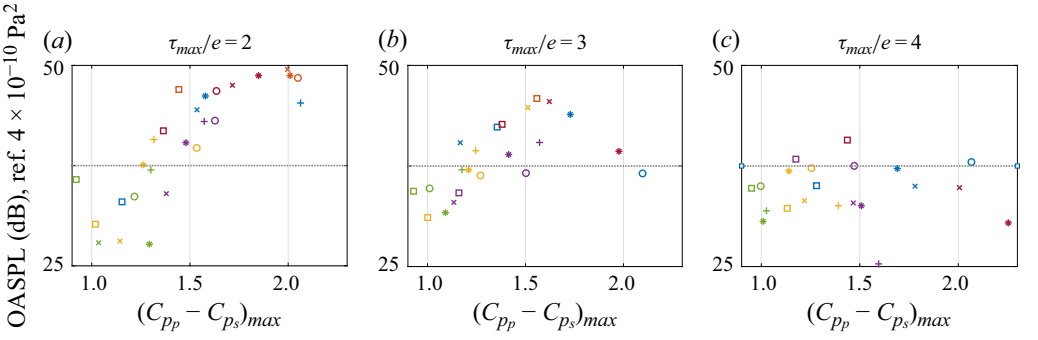

Figure 16. Overall sound pressure levels evaluated in the frequency range of the first tip noise source against the maximum difference between C_{p_p} and C_{p_s}, for different configurations characterised by $\tau_{max}/e = 2$ (*a*), 3 (*b*) and 4 (*c*). The markers refer to the aerofoils: plus, 5505, circle, 5507, asterisk, 5510; cross, 5512; square, 5515. The colours refer to the angles of attack: 7° (□), 10° (—), 12° (—), 15°(—), 17° (—), 20° (—).

thickness-to-gap ratio: 2 for the 5505 aerofoil and 4 for the 5510 profile. The thickness-to-gap ratio determines whether the tip flow remains separated or reattaches to the aerofoil: for $\tau_{max}/e = 2$, the flow remains separated leading to the formation of the first noise source; for $\tau_{max}/e = 4$, the flow reattaches preventing the formation of the low-velocity region. This aligns with the findings of Saraceno *et al.* (2024*b*), which showed the absence of the low-velocity region within the gap for the case with $\tau_{max}/e = 4$.

The two cases analysed in this section were selected to show the influence of the thickness-to-gap ratio on the development of the first tip noise source, as they are characterised by similar pressure distribution along the chord, resulting in the same vortex detachment position. Figures 11(*a*) and 11(*b*) have been expanded by considering different aerofoils, obtaining the three plots shown in figure 16. In figure 16(*a*), the data characterised by $\tau_{max}/e = 2$ follow a proportional trend above the dotted line, but appear sparse below it, as expected, since the first noise source tends to disappear for small angles of attack ($\alpha < 10°$). A similar trend is observed for the cases with $\tau_{max}/e = 3$, shown in figure 16(*b*), with lower values of the maximum strength of the noise source. Almost all data points are found below the dotted line for the cases with $\tau_{max}/e = 4$ in figure 16(*c*). Therefore, we can conclude that the first tip noise source can develop when $\tau_{max}/e < 4$ and

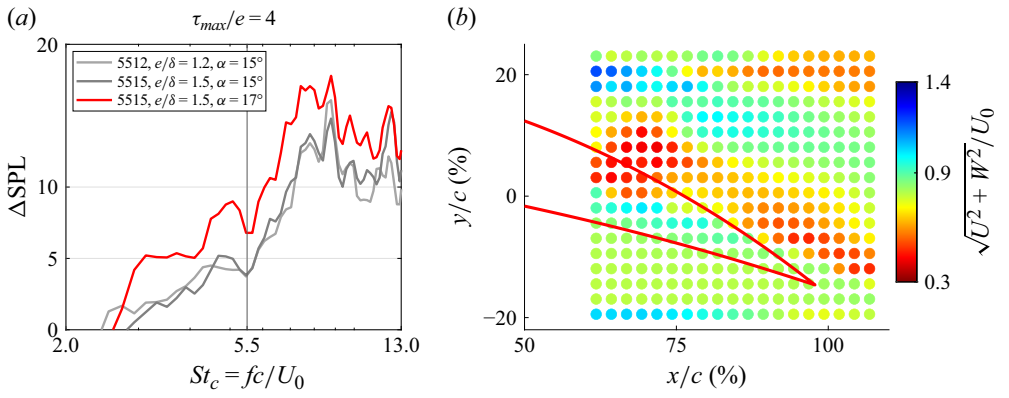

Figure 17. (*a*) Tip leakage noise measured for configurations with $\tau_{max}/e = 4$. (*b*) Mean velocity field of the resultant velocity in the $x-z$ plane measured within the gap for the configuration with $\tau_{max}/e = 4$, NACA 5515 aerofoil and $\alpha = 17°$.

depending on the location of the vortex, a function of the angle of attack. Unfortunately, $\tau_{max}/e \geqslant 4$ cannot be considered as a condition that prevents the formation of the first noise source. Furthermore, the tip flow behaviour appears independent of the boundary layer as figures 16(*b*) and 16(*c*) contain cases with and without the tip immersed within the boundary layer. However, a more detailed analysis of the boundary layer is presented in § 5.

Figure 17(*a*) displays the tip leakage noise obtained for three different configurations with NACA 5512 and 5515, where the gap size was chosen to maintain $\tau_{max}/e = 4$, the identified threshold for the development of the first noise source. At an angle of attack of $\alpha = 15°$, the grey spectral humps nearly collapse within $St_c = 2-5.5$, reaching a negligible peak of about 5 dB. However, a slight increase in the angle of attack to 17° results in the characteristic spectral hump (–). For this configuration with $\tau_{max}/e = 4$ and $\alpha = 17°$, the low-velocity region is found at around 60 % of the chord, as shown in figure 17(*b*), which illustrates the velocity field within the gap. At this position, far from the location with maximum thickness localised at 30 % of the chord, the ratio between the local thickness and the gap size assumes values less than 4, for which the tip flow remains separated until the gap exit. In summary, it is not possible to determine in advance whether the first noise source will develop solely based on the ratio $\tau_{max}/e \geqslant 4$. It is necessary to evaluate the local thickness-to-gap ratio at the location where the tip vortex detaches.

4.2. *Second tip noise source*

The scatter plots of figures 12 (*a*) and 12(*b*) suggested a proportionality between the lift coefficient and the strength of the second tip noise source. Specifically, these data points were obtained using the 5510 aerofoil, where the gap size was changed. Figure 17(*a*) also illustrates the noise increase due to this noise source, within $St_c = 5.5-13$, for the configurations with two different aerofoils and two angles of attack, 5512–5515 and $\alpha = 15°$–17°. Notably, for a fixed τ_{max}/e, the noise source strength is primarily governed by the angle of attack: for the same angle of attack, the two grey lines, corresponding to cases with different aerofoils, collapse well, while as the angle of attack increases the noise levels increase.

This dependency is further explored in figure 18, where the strength of the second tip noise source is plotted against the lift coefficient for a variety of aerofoils, ranging from the thinnest 5505 to the thickest 5520. Each scatter plot corresponds to a specific τ_{max}/e

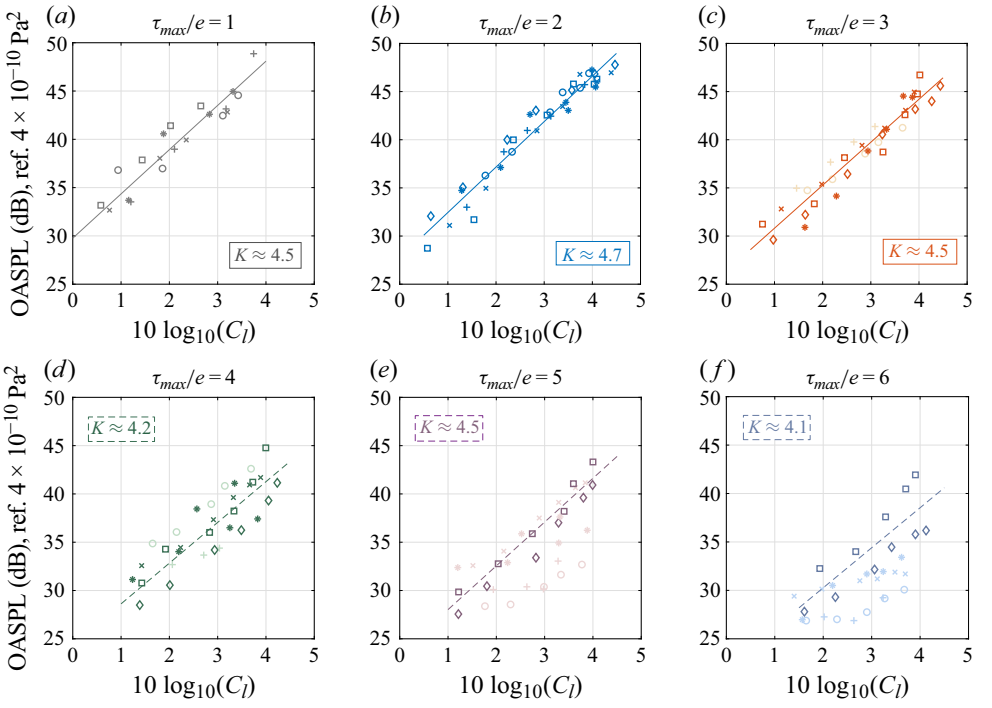

Figure 18. Overall sound pressure levels evaluated in the frequency range of the second noise source against the lift coefficient C_l measured for different configurations with $\tau_{max}/e = [1, 6]$. The markers refer to the NACA aerofoils: plus, 5505; circle, 5507; asterisk, 5510; cross, 5512; square, 5515; diamond, 5520. Muted colours refer to the configurations with the aerofoil tip immersed in the wall boundary layer with $e/\delta < 1$. Specifically, 5505 and 5507 with $e/\delta = 0.66$ and 0.92 (c); 5505 and 5507 with $e/\delta = 0.5$ and 0.7 (d); 5505, 5507, 5510 and 5512 with $e/\delta = 0.4$, 0.56, 0.8 and 0.96 (e); 5505, 5507, 5510 and 5512 with $e/\delta = 0.33$, 0.46, 0.66 and 0.8 (f).

ratio, with the gap size adjusted accordingly. For each plot, the data points are distributed linearly, increasing with the lift coefficient. An empirical power relationship can be defined as $\overline{p'^2} \propto {C_l}^K$, where $\overline{p'^2}$ is the mean square of the fluctuating pressure linked to the second tip noise source, C_l is the lift coefficient measured at the tip and K is the slope of the least-squares line superimposed on the scatter plots. The slope K remains almost constant for $\tau_{max}/e = 1$, 2 and 3. For $\tau_{max}/e \geqslant 4$, the dispersion of the data increases with a consequent decrease in the slope. This effect can be due to the immersion of the aerofoil tip within the boundary layer, rather than a change in the tip flow behaviour associated with the τ/e ratio. By removing all the configurations characterised by $e/\delta < 1$ (muted colours in the figure), the dashed least-square lines present a slope K that aligns closely with that obtained for $\tau_{max}/e < 4$, suggesting a significant role of the boundary layer. Due to the linear relationship between C_l and V_L shown in figure 13, the power law can be expressed as $\overline{p'^2} \propto {V_L}^{4.5}$, which is close to the V_∞^5 scaling law characteristic of a dipole source close to a sharp edge (Howe 2002). This suggests that the observed slope may be a consequence of the dipole nature of the second tip noise source. The power relationship is then finalised as $\overline{p'^2} = a{C_l}^{4.5}$, where the coefficient a depends on the thickness-to-gap ratio, decreasing as τ_{max}/e increases. Ideally, when the thickness-to-gap ratio tends to infinity (with the gap size approaching zero), the tip flow does not enter the gap, thereby preventing the development of the second noise source.

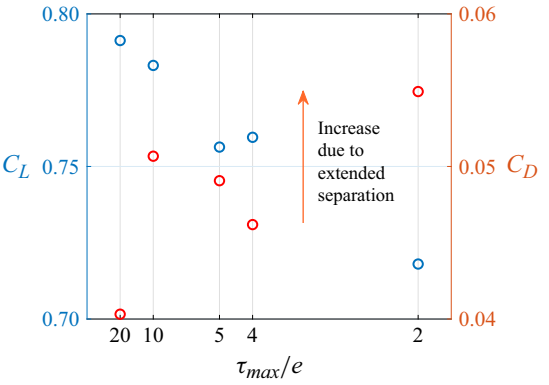

Figure 19. Variation of the lift and drag coefficients, C_L and C_D, with the non-dimensional gap size τ_{max}/e, considering NACA 5510 aerofoil with a geometric angle of attack $\alpha = 15°$.

The second tip noise source develops whenever the tip flow separates at the pressure side edge singularity, regardless of whether the tip flow reattaches to the aerofoil or remains separated until exiting the gap. This behaviour is reflected in the power relationship between the strength of the noise source and the lift coefficient, where the slope remains independent of the thickness-to-gap ratio. The dipole nature of the source dictates the slope value. However, as the thickness-to-gap ratio increases and the aerofoil tip is more immersed in the boundary layer, the noise strength decreases.

The power relationship between the intensity of the second tip noise source and the lift coefficient is useful during the design process, as it allows for a qualitative prior estimation of the noise intensity based on the τ_{max}/e ratio and the lift coefficient C_l. The lift coefficient can be obtained by integrating the pressure coefficient C_p at either the midspan or the aerofoil tip. In particular, knowing C_p at the tip enables the prediction of the TLV detachment location, which, together with the τ_{max}/e ratio, provides insight into the development of the first tip noise source. Future studies with different chamber lines are needed to extend the correlations established in this work.

4.3. *Aerodynamic implications*

This section evaluates the overall aerodynamic performance of the configurations obtained by varying the angle of attack and gap size. Figure 19 displays the lift and drag coefficients, C_L and C_D, as a function of the non-dimensional gap size τ_{max}/e for the configuration with NACA 5510 aerofoil and geometric angle of attack $\alpha = 15°$. In the evaluation of these force coefficients, the effective angle of attack α_{eff}, which results to be approximately one-third of α, was considered to account for wind tunnel deflection (Glegg & Devenport 2017). It can be seen that C_L decreases as the gap increases, i.e. τ_{max}/e decreases, consistent with the findings of Higgens *et al.* (2019) and the considerations of Denton (1993) regarding the drop in lift due to the reduction in the aerofoil spanwise extent. Indeed, as the gap between the aerofoil tip and the casing wall increases, the effective span of the aerofoil decreases. The gap also causes a rise in drag, with a significant increase when e increases from $e = 5$ to 10 mm, i.e. $\tau_{max}/e = 4$ to 2. As observed in the previous section, the first noise source develops when $\tau_{max}/e < 4$, corresponding to a tip flow that does not reattach to the aerofoil surface and remains separated until exiting the gap. Bindon (1989) found that most of the performance loss occurs when the separation bubble is ejected into the gap, corresponding to the tip flow remaining separated. Therefore, this extended separation may contribute to both increased drag and generation of the first tip noise source.

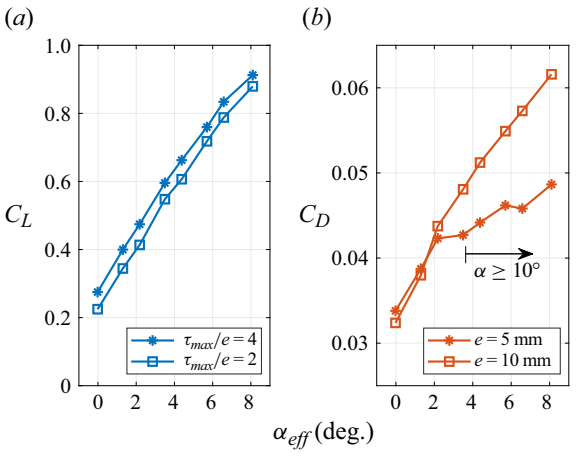

Figure 20. Variation of the lift and drag coefficients, C_L (a) and C_D (b), with the effective angle of attack α_{eff}, considering NACA 5510 aerofoil with $\tau_{max}/e = 2$ and 4.

The development of the first noise source was found to depend on the thickness-to-gap ratio and the geometric angle of attack, as shown in figures 11 and 17. This noise source was not observed when $\tau_{max}/e < 4$ and $\alpha < 10°$, or when $\tau_{max}/e \geqslant 4$ regardless of α. This behaviour helps explain the trend of the drag coefficients plotted against α_{eff} in figure 20(b), measured for two gap sizes $e = 5$ and 10 mm, i.e. $\tau_{max}/e = 4$ to 2. The drag coefficients remain similar at small angles of attack but begin to diverge at a certain α_{eff}, which corresponds to $\alpha = 10°$, the point at which the first noise source develops for $\tau_{max}/e = 2$. At higher angles of attack, the drag produced in the case with $\tau_{max}/e = 2$ is higher than that of the small gap. The lift forces, shown in figure 20(a), follow a linear trend with the effective angle of attack, with slightly higher values for the smaller gap, as expected from figure 19.

In summary, this section highlights that drag losses are connected to the tip flow behaviour and, similarly to the first noise source, depend on the angle of attack and the thickness-to-gap ratio. This suggests a relationship between the first noise source and drag losses, indicating that optimising one can improve both aerodynamic performance and noise reduction in turbomachinery design.

5. Effect of the boundary layer e/δ

In the previous section, the boundary layer was observed to influence the strength of the second tip noise source. The slope of the least-squares lines in figure 18 decreases due to the wider spread of the data for the cases with aerofoil tips immersed within the boundary layer. This effect of the boundary layer was significant for $\tau_{max}/e \geqslant 4$, as figure 18(c) with $\tau_{max}/e = 3$ includes data obtained with the aerofoil tip immersed in the boundary layer (Specifically, NACA 5505 and 5507 with $e/\delta = 0.66$ and 0.92) that align well with the overall linear trend. However, for these cases, the boundary-layer thickness was set to $\delta = 5$ mm. The two cases previously analysed in detail, with 5510 aerofoil, $\alpha = 15°$, $\tau_{max}/e = 2$ and 4, have been immersed in a thicker boundary layer of $\delta = 20$ mm, both resulting in $e/\delta < 1$. Figure 21 shows that the reduction in the strength of the second noise source, when τ_{max}/e increases from 2 to 4, is more pronounced in a thicker boundary layer, i.e. $e/\delta < 1$. This greater reduction can be attributed to the significantly lower tip flow velocity that can be achieved in a thicker boundary layer.

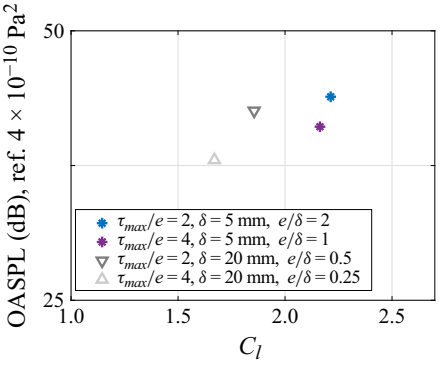

Figure 21. Overall sound pressure levels evaluated in the frequency range of the second noise source against the lift coefficient C_l for four configurations with $\tau_{max}/e = 2$ and 4 and boundary layer thickness $\delta = 5$ and 20 mm. These configurations are characterised by the same aerofoil 5510 and angle of attack $\alpha = 15°$.

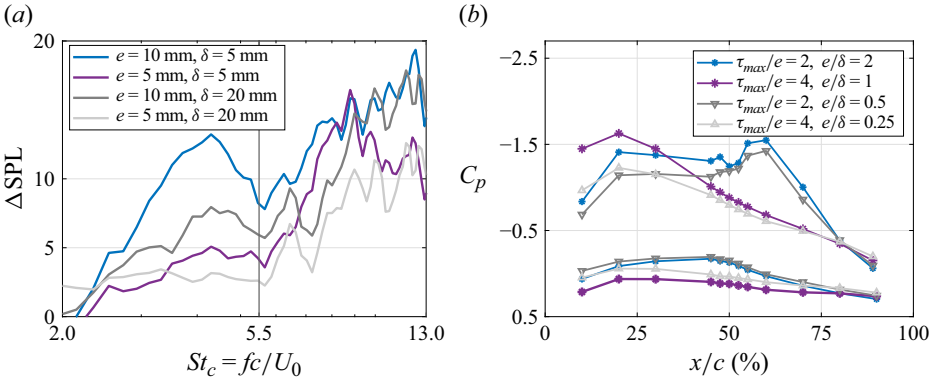

Figure 22. (*a*) Tip leakage noise and (*b*) pressure distributions C_p along the aerofoil measured for four configurations with $\tau_{max}/e = 2$ and 4 and boundary-layer thickness $\delta = 5$ and 20 mm. These configurations are characterised by the same aerofoil 5510 and angle of attack $\alpha = 15°$.

Figure 21 also shows a decrease in the lift coefficient as the boundary-layer thickness increases, for the configurations with the same τ_{max}/e. This is due to a reduction in the loading on the aerofoil suction side, especially upstream of the midchord, while the pressure coefficient on the pressure side remains almost constant, as illustrated in figure 22(*b*). Both cases with $\tau_{max}/e = 2$ are characterised by a pressure peak in the pressure distribution at $x/c = 60$ %, with its magnitude slightly reduced for the case with a thicker boundary layer. Due to the link between the magnitude of the pressure peak and the intensity of the first tip noise source, a shallower peak of almost 8 dB is measured, as shown within $St_c = 2{-}5.5$ in figure 22(*a*) for the case $e/\delta = 0.5$ (–). The other cases, with $\tau_{max}/e = 4$, remain characterised by the absence of the first tip noise source.

6. Conclusions

The current investigation has identified three key non-dimensional parameters influencing the tip leakage noise, one of the least understood noise sources in turbomachinery. Specifically, the angle of attack α, the ratio between the maximum aerofoil thickness and gap size τ_{max}/e and the ratio between the gap size and boundary-layer thickness e/δ are

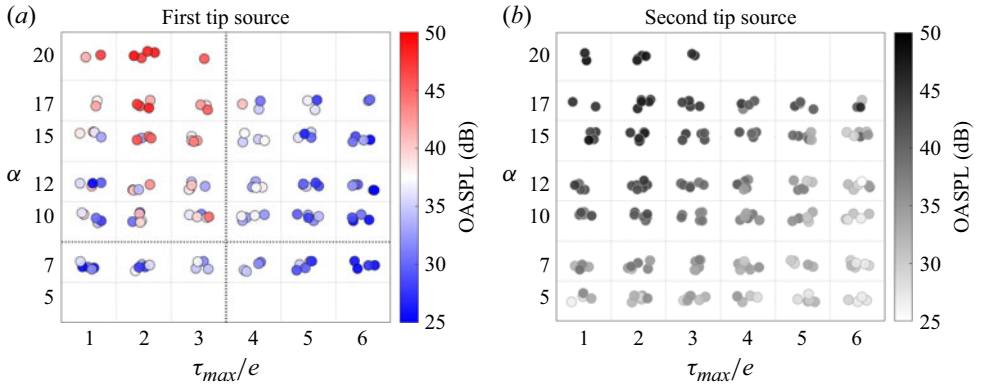

Figure 23. Correlation maps illustrating the relationship between the strength of the first (*a*) and second (*b*) tip leakage noise sources and the non-dimensional parameters α and τ_{max}/e. The effect of e/δ is less evident. The diverging colourmap in (*a*) highlights the conditions under which the first noise source disappears, with blue indicating its absence. The gradient colourmap in (*b*) shows how the strength of the second noise source varies, increasing from white to black.

the parameters that mostly control the two fluid-dynamic instabilities, vortex shedding and shear-layer roll-up, responsible for the two tip leakage noise sources. A wide range of configurations, obtained by varying α and e and using aerofoils with different τ_{max}, have been experimentally analysed through steady and unsteady pressure measurements, hot-wire velocity measurements in a midgap plane and along the aerofoil suction side region, as well as aerodynamic force measurements. The effect of the boundary layer has been investigated by considering two boundary-layer thicknesses.

The correlation map in figure 23(*a*) illustrates the relationship between the strength of the first noise source and the two non-dimensional parameters τ_{max}/e and α, highlighting the conditions under which this source disappears. The effect of e/δ on this source is less evident. To ensure an intuitive interpretation, a diverging colourmap was used, with blue representing the absence of the noise source and red indicating its presence and increasing strength. This study established that the first tip noise source emerges when the conditions $\tau_{max}/e < 4$ and $\alpha \geqslant 10°$ are met. In this regime, the tip flow separates at the aerofoil pressure side edge and does not reattach. Specifically, this extended separated flow develops when the TLV detaches from the aerofoil surface. The location of this vortex detachment can be identified by the minimum pressure peak observed in the C_p pressure distribution along the aerofoil suction-side tip, which varies with α and e. Additionally, the magnitude of this peak, a function also of e/δ, is directly related to the strength of the first noise source. Overall, this source tends to disappear for $\alpha < 10°$ and $\tau_{max}/e \geqslant 4$; however, to confirm this, it is necessary to analyse the local ratio τ/e at the position of the vortex detachment.

The correlation plot in figure 23(*b*) with gradient colourmap provides a clear visualisation of how the strength of the second noise source increases with α and its attenuation as τ_{max}/e increases. The second tip noise source is associated with shear-layer roll-up, which occurs whenever the tip flow separates at the pressure side edge. This characteristic is reflected in the following scaling law, where slope is independent of τ_{max}/e: $\overline{p'^2} \propto C_l{}^{4.5}$, with $\overline{p'^2}$ representing the pressure fluctuations associated with the second tip noise source, C_l the lift coefficient function of the angle of attack and the exponent 4.5 reflecting the dipole nature of the source. However, the noise strength decreases as the aerofoil tip becomes more immersed in the boundary layer and the

thickness-to-gap ratio increases, ideally approaching zero as τ_{max}/e tends to infinity. This study also highlights that, while the lift coefficient C_l remains consistent whether evaluated at midspan or at the tip, the C_p pressure distribution at the tip provides valuable information about the tip flow topology and vortex, and, consequently, about the first tip noise source.

In addition to these noise sources, the aerodynamic forces acting on the aerofoil were evaluated by varying the angle of attack and gap size. The lift curve shows a linear trend with the angle of attack, decreasing as the gap increased. On the contrary, drag is influenced by the behaviour of the tip flow, depending not only on the angle of attack but also on the thickness-to-gap ratio. Higher drag losses are observed in the presence of the extended separated flow, which is also responsible for the first tip noise source.

Acknowledgements. The first author would like to thank Professor Hirschberg for the inspiring conversation that contributed to the development of this study, Dr S. Palleja-Cabre and J. Ballgjati for assistance with data acquisition, Professor P. Joseph for insightful conversations and Rolls-Royce for continued technical support.

Funding. The authors would like to acknowledge the financial support of the Royal Academy of Engineering (RF\201819\18\194).

Declaration of interests. The authors report no conflict of interest.

Data availability statement. The data that support the findings of this study are available upon request.

Author contributions. I. Saraceno: Conceptualisation, Formal analysis, Investigation, Writing – original draft, Writing – review and editing. P. Chaitanya: Conceptualisation, Investigation, Funding acquisition, Writing – review and editing. B. Ganapathisubramani: Conceptualisation, Investigation, Writing – review and editing.

References

ANDERSON, J.D. 2001 *Fundamentals of Aerodynamics*. McGraw-Hill.

BINDON, J.P. 1989 The measurement and formation of tip-clearance loss. *J. Turbomach.* **111**, 257–263.

CAMUSSI, R., GRILLIAT, J., CAPUTI-GENNARO, G. & JACOB, M.C. 2010 Experimental study of a tip leakage flow: wavelet analysis of pressure fluctuations. *J. Fluid Mech.* **660**, 87–113.

CHONG, T.P., JOSEPH, P. & DAVIES, P.O.A.L. 2009 Design and performance of an open jet wind tunnel for aero-acoustic measurements. *Appl. Acoust.* **70**, 605–614.

DAMBACH, R. & HODSON, H.P. 2001 Tip leakage flow in axial compressors. *J. Propul. Power* **17**, 644–650.

DENTON, J.D. 1993 Loss mechanisms in turbomachines. *J. Turbomach.* **115**, 621–656.

DRELA, M. 1989 Xfoil: An analysis and design system for low reynolds number airfoils. In *Low Reynolds Number Aerodynamics*, Springer.

GANZ, U.W., JOPPA, P.D., PATTEN, T.J. & SCHARPF, D.F. 1998 Boeing 18-inch fan rig broadband noise test, *Tech. Rep.* 208704. NASA.

GLEGG, S. & DEVENPORT, W. 2017 *Aeroacoustics of Low Mach Number Flows*. Academic Press.

GRAHAM, J.A.H. 1986 Investigation of a tip clearance cascade in a water analogy rig. *J. Engng Gas Turbines Power* **108**, 38–46.

GRILLIAT, J., JACOB, M.C., CAMUSSI, R. & CAPUTI-GENNARO, G. 2007 Tip leakage experiment – part one: Aerodynamic and acoustic measurements. In *13th AIAA/CEAS Aeroacoustics Conference*. AIAA 2007-3684.

HIGGENS, A., JOSEPH, P., LIDTKE, A.K. & TURNOCK, S.R. 2019 Investigation into the tip-gap flow and its influence on ducted propeller tip- gap noise using acoustic analogies. *J. Ship Res.* **00**, 1–16.

HOWE, M.S. 2002 *Theory of Vortex Sound*. Cambridge University Press.

INTARATEP, N. 2006 Formation and development of the tip leakage vortex in a simulated axial compressor with unsteady inflow PhD thesis, Virginia Polytechnic Institute, USA.

JACOB, M.C., GRILLIAT, J., CAMUSSI, R. & GENNARO, G.C. 2010 Aeroacoustic investigation of a single airfoil tip leakage flow. *Intl J. Aeroacoust.* **9**, 253–272.

JACOB, M.C., JONDEAU, E. & LI, B. 2016*a* Time-resolved piv measurements of a tip leakage flow. *Intl J. Aeroacoust.* **15**, 662–685.

JACOB, M.C., JONDEAU, E., LI, B. & BOUDET, J. 2016*b* Tip leakage flow: Advanced measurements and analysis. In *22nd AIAA/CEAS Aeroacoustics Conference*. AIAA 2016-2823.

KANG, S. & HIRSCH, C. 1993 Experimental study on the three-dimensional flow within a compressor cascade with tip clearance: part i – velocity and pressure fields. *J. Turbomach.* **115**, 435–443.

KANG, S. & HIRSCH, C. 1994 Tip leakage flow in linear compressor cascade. *J. Turbomach.* **116**, 657–664.

KOCH, R., SANJOSÉ, M. & MOREAU, S. 2021 Large-eddy Simulation of a single airfoil tip-leakage flow. *AIAA J.* **59**, 2546–2557.

KUNDU, P.K., COHEN, I.M. & DOWLING, D.R. 2016 *Fluid Mechanics (6th edn)*. Academic Press.

LIU, Y., WANG, Z.N., TAN, L., TUCKER, P.G. & MOLLER, F.M. 2024 Tip-leakage-flow unsteadiness and associated control. *Phys. Fluids* **36**, 055156.

MOORE, J. & TILTON, J.S. 1988 Tip leakage flow in a linear turbine cascade. *J. Turbomach.* **110**, 18–26.

RAINS, D. 1954 Tip clearance flow in axial compressors and pumps. Phd thesis, California Institute of Technology, USA.

SARACENO, I., CHAITANYA, P., GANAPATHISUBRAMANI, B., ALGUACIL, A., MOREAU, S. & SANJOSE, M. 2024*a* On the numerical investigation of the tip leakage noise sources of a stationary aerofoil. In *30th AIAA/CEAS Aeroacoustics 2024 Conference*. AIAA 2024-3116.

SARACENO, I., CHAITANYA, P., JAISWAL, P., PALLEJA-CABRE, S., LONG, W. & GANAPATHISUBRAMANI, B. 2024*b* On the tip leakage noise mechanisms of a stationary aerofoil.

STORER, A.J. & CUMPSTY, N.A. 1991 Tip leakage flow in axial compressors. *J. Turbomach.* **113**, 252–259.

ZHANG, B., LIU, B., MAO, X., WANG, H., YANG, Z. & LI, Z. 2022 Interaction mechanism between the tip leakage flow and inlet boundary layer in a highly loaded compressor cascade based on scale-adaptive simulation. *Phys. Fluids* **34**, 116112.